Phase transitions and magnetic domain coexistence in $Nd_{0.5}Sr_{0.5}MnO_3$ thin films

I-Ting Chiu[a], Alexander M. Kane[b], Rajesh V. Chopdekar[c], Peifen Lyu[b], Apurva Mehta[d], Chris M. Rouleau[e], Alpha T. N'Diaye[c], Elke Arenholz[c,f], Yayoi Takamura[b,*]

[a] Department of Chemical Engineering, University of California, Davis, Davis, CA 95616, United States
[b] Department of Materials Science and Engineering, University of California, Davis, Davis, CA 95616, United States
[c] Advanced Light Source, Lawrence Berkeley National Laboratory, Berkeley, CA 94720, United States
[d] Stanford Synchrotron Radiation Lightsource, SLAC National Accelerator Laboratory, Menlo Park, CA 94025, United States
[e] The Center for Nanophase Materials Sciences, Oak Ridge National Laboratory, Oak Ridge, TN 37830, United States
[f] Cornell High Energy Synchrotron Source, Cornell University, Ithaca, NY 14853, United States

A B S T R A C T

We present a study of the physical properties of perovskite oxide $Nd_{0.5}Sr_{0.5}MnO_3$ (NSMO) thin films grown on (110)-oriented $SrTiO_3$ substrates. In bulk form, NSMO displays coupled magnetic and electronic transitions from paramagnetic/insulator to ferromagnetic (FM)/metal and then to antiferromagnetic (AFM)/charge-ordered insulator with decreasing temperature. In thin films, the AFM ordering only occurs when the films exist in an anisotropic strain state such as those obtained on (110)-oriented cubic substrates. In this work, resonant X-ray reflectivity, soft X-ray photoemission electron microscopy (X-PEEM), and magnetometry measurements showed that the NSMO film displays both vertical and lateral magnetic phase separation. Specifically, the film consists of three layers with different density and magnetic properties. The FM and AFM properties of the main NSMO layer were probed as a function of temperature using soft X-ray magnetic spectroscopy, and the coexistence of lateral FM and AFM domains was demonstrated at 110 K using X-PEEM.

1. Introduction

In order to maintain the current pace of innovation in memory and logic devices, novel classes of materials and alternative device designs are imperative for further breakthroughs [1]. Among the candidate materials, complex metal oxides (CMOs) are promising due to their diverse functional properties such as colossal magnetoresistance, abrupt metal-to-insulator transitions, and a high degree of spin polarization at the Fermi level [2–9]. Within the family of CMOs, perovskite oxides with the chemical formula ABO_3 have received a great deal of interest because of the wide range of functional properties which can be controlled through chemical substitutions on the A and B sites, as well as the oxygen stoichiometry [10–13]. In addition, modern thin film synthesis techniques have enabled fine control of structural parameters such as the epitaxial strain state, strain symmetry, and film thickness such that artificial composite materials with emergent functional properties at interfaces can be investigated [14–16].

For example, the hole-doped manganite $Nd_{1-x}Sr_xMnO_3$ displays a rich phase diagram of different magnetic and electronic phases depending on the Sr doping level. For a small range of compositions from $0.48 < x < 0.51$, $Nd_{0.5}Sr_{0.5}MnO_3$ (NSMO), two coupled magnetic and electronic transitions are observed as a function of temperature, involving a first transition upon cooling from the paramagnetic (PM)/insulating phase to a ferromagnetic (FM)/metallic phase at ~197 K, followed by a transition to an antiferromagnetic (AFM)/charge-ordered insulating phase at ~150 K [17]. Over a range of applied magnetic field and temperatures, first order phase transitions can lead to coexistence of the FM and AFM phases [18–20]. Recent studies show that this magnetic phase coexistence can lead to large magnetoresistance effects which can be applied in hard disk drives and magnetoresistive spintronic device applications [21–25].

In NSMO thin films, it has been reported that stabilizing the AFM/insulator phase requires an anisotropic strain state to support Jahn-Teller (JT) distortions of the MnO_6 octahedra and the structural freedom to drive the Mn^{3+} ions into the charge-ordered phase [26–28]. Such an anisotropic strain state can be achieved using (110)-oriented substrates such that the *a*- and *b*-axes of the pseudocubic (pc) unit cell are canted 45° out of the (110) surface plane, creating some freedom for the BO_6 octahedral bond directions to distort at temperatures below the Néel temperature (T_N). This substrate orientation presents a rectangular growth surface where the two low-index in-plane directions are the [0 0 1] and [1 $\bar{1}$ 0] cubic substrate directions. Bulk NSMO has orthorhombic symmetry with lattice parameters of $a = 0.543$ nm, $b = 0.548$ nm, and $c = 0.764$ nm at room temperature, corresponding

* Corresponding author.
E-mail address: ytakamura@ucdavis.edu (Y. Takamura).

https://doi.org/10.1016/j.jmmm.2019.166116

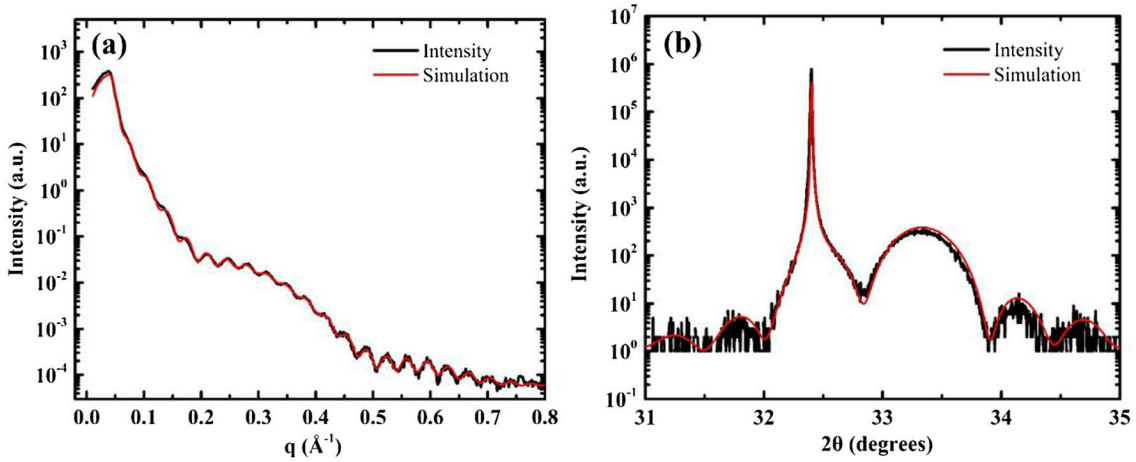

Fig. 1. (a) RXRR spectrum and (b) XRD ω-2θ scan around the substrate (1 1 0) peak for an NSMO film on (1 1 0)-oriented STO substrate. Black and red curves are the raw data and simulations, respectively. (For interpretation of the references to colour in this figure legend, the reader is referred to the web version of this article.)

to a_{pc} = 0.3840 nm [17,29]. On (1 1 0)-oriented $SrTiO_3$ (STO) substrates with cubic symmetry and a = 3.905 Å, the lattice mismatch between STO and the NSMO film is 0.86% in the [0 0 1] substrate direction and 2.23% in [1 $\bar{1}$ 0] substrate direction, which are expected to result in fully strained and partially relaxed strain states, respectively [28]. In contrast, when NSMO films are grown on (0 0 1)-oriented substrates where the *a*- and *b*-axes of the pseudocubic unit cell are clamped to the substrate, only the FM/metallic phase is observed down to low temperatures [26,28]. Furthermore, prior studies have shown that stabilizing the AFM/insulator phase in NSMO thin films strongly depends on the preparation method or growth conditions, such as substrate temperature and oxygen pressure during pulsed laser deposition (PLD) [26–28,30–32].

In this work, we present a study of the physical properties of NSMO thin films grown on (1 1 0)-oriented STO substrates. Resonant X-ray reflectivity (RXRR) and bulk magnetization measurements showed that vertically the NSMO film consists of three layers which differ in terms of their density and magnetic properties. Polarized soft X-ray magnetic spectroscopy, exploiting the X-ray magnetic circular/linear dichroism (XMCD/XMLD) effects, were performed to directly probe both the FM and AFM characteristics, respectively, and to confirm the occurrence of the FM-AFM transition. X-ray photoemission electron microscopy (X-PEEM) was used to image the FM and AFM domains and to demonstrate the lateral coexistence of FM and AFM domains at 110 K, as expected for a first order phase transition. These characterization techniques demonstrate the multiple magnetic and electronic phase transitions in the NSMO films, and thus the possibility and diversity of functional properties to be applied in next generation devices.

2. Experimental methods

Epitaxial NSMO thin films were deposited on (1 1 0)-oriented STO substrates by PLD with a laser pulse frequency of 5 Hz and laser fluence of ~1.5 J cm^{-2}. During the growth, the substrate temperature was held at 750 °C and the oxygen background pressure was 160 mTorr. The films were cooled slowly to room temperature after the deposition with an oxygen pressure of 100 Torr to ensure proper oxygen stoichiometry. The structural properties of the films were characterized by high-resolution X-ray diffraction (XRD) using a Bruker D8 DISCOVER four-circle diffractometer using Cu $K_{\alpha 1}$ X-rays. RXRR spectra were obtained at Beamline 2-1 at the Stanford Synchrotron Radiation Lightsource using an X-ray energy near the Mn *K* edge (6552 eV). This K-edge absorption energy was obtained by doing the Kramers-Kronig transformation to the X-ray absorption near edge structure energy spectra, where the real part of the X-ray dispersion correction factor, *f′*, is at a minimum. XRR spectra taken at resonant energies provide increased sensitivity to the chemical contrast between thin films and substrates which have similar density [33]. By simulating the RXRR spectra in the GenX reflectivity simulation software [34], the thickness, roughness, and density values of the films were modeled. A Lakeshore probe station was used to measure the film resistivity upon warming from 80 K with the van der Pauw geometry. The bulk magnetic properties with the magnetic field applied along the in-plane [0 0 1] substrate direction was measured using a VersaLab Physical Properties Measurement System from Quantum Design.

Soft X-ray magnetic spectroscopy at the Mn *L*-edge was performed at 80 K and 160 K at beamlines 4.0.2 and 6.3.1 at the Advanced Light Source (ALS) using the total electron yield (TEY) detection mode. For the XMCD measurements, the X-rays were incident upon the sample at a 30° grazing angle along the [0 0 1] substrate directions, and the magnetic field was applied parallel to the X-rays. The dichroism was calculated as the difference between spectra captured with applied magnetic field ± 1.4 T. The X-ray linear dichroism (XLD) spectra were acquired with an X-ray incidence angle of 45° along the [1 $\bar{1}$ 0] substrate directions using *s*- and *p*-polarized X-rays so that the ***E***-vector was oriented parallel to the [0 0 1] and [1 0 0] substrate directions, respectively. The XLD spectra were calculated as the difference of the XA spectra obtained with the two linear polarizations. The X-PEEM images were acquired using the PEEM3 microscope at Beamline 11.0.1 at the ALS [35], with the X-ray beam incident along the [0 0 1] substrate direction at a 30° grazing incidence angle. XMCD-PEEM images were obtained using right/left circularly polarized (RCP/LCP) X-rays at the photon energy corresponding to the maximum XMCD signal. XLD-PEEM images were acquired at the photon energies corresponding to the negative and positive features of the Mn L_2 XLD spectra with the polarization rotating from *p*- to *s*-polarized X-rays. In all cases, the domain images were obtained using an asymmetry equation, $I = (I_{RCP} - I_{LCP})/(I_{RCP} + I_{LCP})$, to remove topographic contributions and work function differences from the domain images.

3. Results and discussion

RXRR and XRD ω-2θ scans (Fig. 1) display a well-defined film peak and Kiessig fringes indicative of a highly crystalline film with smooth interfaces. From the XRD data, a_{pc}(NSMO) is determined to be 0.3825 nm, consistent with a film under substrate-induced tensile strain. The periodicity of the Kiessig fringes in the RXRR spectrum (Fig. 1a) corresponds to a total film thickness of 16.5 nm, however, an envelope of a longer period oscillation indicates that the NSMO film is best represented as three layers which differ by their density due to

Table 1
Optimized fit parameters for RXRR spectra.

	Thickness (nm)	Roughness (nm)	Density (g cm^{-3})
Carbon layer	1.00 ± 0.32	0.31 ± 0.03	2.36 ± 0.06
NSMO_surface	0.84 ± 0.01	0.80 ± 0.10	6.30 ± 0.04
NSMO_main	14.74 ± 0.11	0.57 ± 0.04	6.40 ± 0.03
NSMO_interface	0.93 ± 0.02	0.66 ± 0.05	6.32 ± 0.02
STO substrate	–	0.27 ± 0.02	5.12 ± 0.00

changes in their composition, electronic properties, and/or optical constants. Table 1 lists the full structural characteristics of these three layers. Similar three-layer models have been used for other oxide thin films [30,36]. Due to the exposure of the samples to atmosphere between deposition and X-ray measurements, a thin surface carbon-containing layer was added to refine the simulation [37]. The error bars were determined by the range that produces a ± 5% change in the figure of merit (FOM). The lower density in the layer at the NSMO/STO interface may result from the tensile strain induced by the STO substrate, while the thin surface layer may be slightly oxygen or cation deficient [36,38,39]. The main NSMO layer (thickness ~14.7 nm) has the same density as bulk NSMO and is sandwiched between the surface and interface layers. Compared to simpler two-layer models with only the surface and the main layer, or the main and substrate interface layers (see Fig. S1), the logarithmic FOM of the three-layer model is decreased by 59% and 46%, respectively (FOM = 0.05378). The surface and interface layers are not detectable in the ω-2θ scan due to their small thickness (< 1 nm).

Reciprocal space maps (RSMs) taken around the asymmetric (2 2 2) and (3 1 0) peaks for the STO substrate are shown in Fig. 2. As discussed earlier, it has been postulated that the asymmetric strain state of NSMO thin films grown on (1 1 0)-oriented STO substrates [26,28] facilitates the observation of the FM-AFM transition. According to this theory, the films need to be strained to the substrate in the in-plane [0 0 1] direction (corresponding to the (2 2 2) peak) and partially relaxed in the in-plane [1 $\bar{1}$ 0] direction (corresponding to the (3 1 0) peak). As shown in Fig. 2, the NSMO film adopts this epitaxial strain state, as the weak film peak is shifted to higher values of reciprocal space compared to the substrate peak in the (3 1 0) RSM, while the two peaks are exactly vertically aligned in the (2 2 2) RSM.

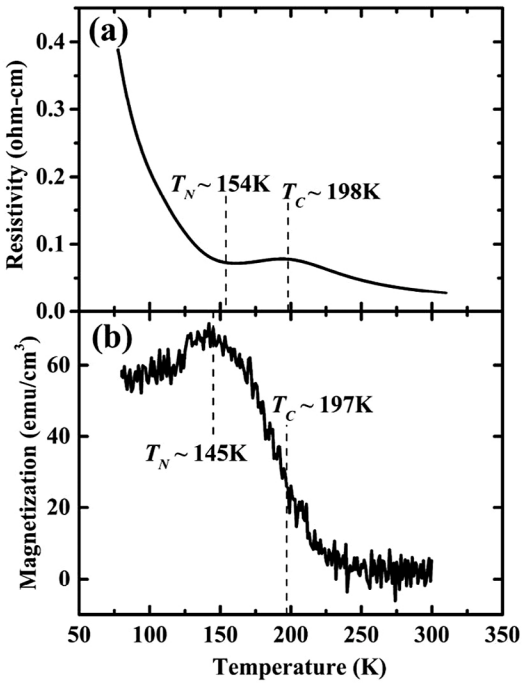

Fig. 3. (a) Film-averaged resistivity and (b) magnetization as a function of temperature, measured along the [0 0 1] substrate direction. A magnetic field of 0.06 T was applied during the magnetization measurement.

The bulk magnetic properties of the NSMO thin films were probed using resistivity and magnetization measurements as shown in Fig. 3. These values are normalized to the film volume using the surface area and the total film thickness (16.5 nm) obtained in the RXRR fitting. Upon cooling, the film undergoes two electrical and magnetic phase transitions, i.e. PM/insulator to FM/metal transition at Curie temperature (T_C) ~ 197 K and the FM/metal to AFM/insulator transition at T_N ~ 150 K. In the resistivity measurement, T_C and T_N were determined as the temperature where the curve is a local maximum and minimum, respectively [40–42]. In the magnetization plot, the transition temperatures were determined as the temperatures where dM/dT has the

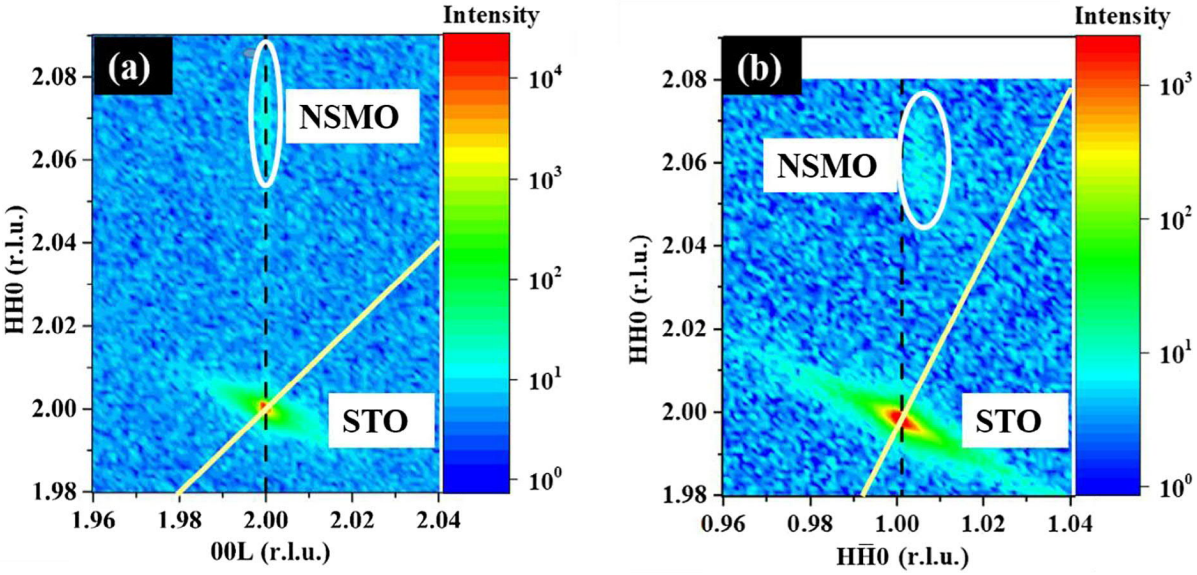

Fig. 2. RSMs around the (a) (2 2 2) peak and (b) (3 1 0) substrate peak for an NSMO film on (1 1 0)-oriented STO substrate. The dashed vertical line represents a fully-strained film while solid white line represents a fully-relaxed film. The circle denotes the location of the film peaks. The film is fully strained in the in-plane [0 0 1] direction while partially relaxed in the in-plane [1 $\bar{1}$ 0] direction.

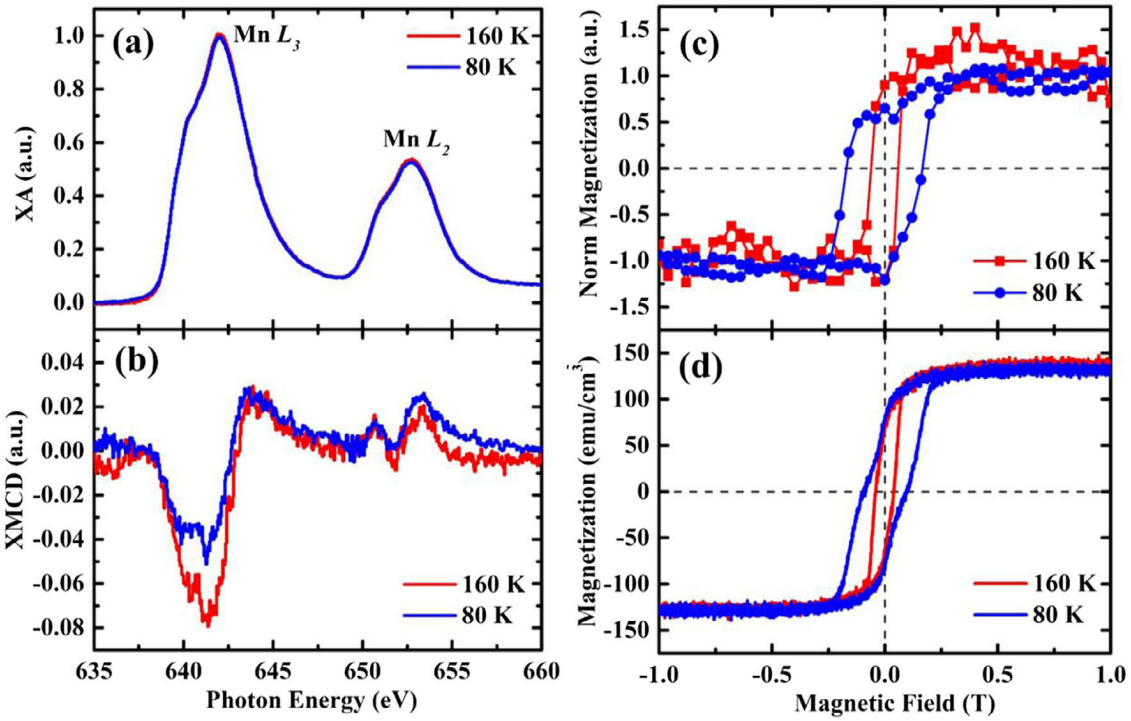

Fig. 4. Mn (a) XA and (b) XMCD spectra taken at 80 K and 160 K with 1.4 T magnetic field in the [0 0 1] substrate direction. (c) Mn-XMCD and (d) bulk magnetic hysteresis loops taken at 80 K and 160 K with the magnetic field applied in the [0 0 1] -direction.

largest magnitude [43]. Using these metrics, the transition temperatures are in good agreement between the two measurements. In the temperature region below T_N, the resistivity exponentially increases with decreasing temperature as expected for an insulating film, however, the magnetization gradually decreases but does not completely drop to zero as would be expected for an AFM phase. This result suggests that instead of displaying complete AFM ordering, the transition at T_N may be associated with a gradual growth of AFM domains with the presence of shrinking FM domains. As the AFM domains grow, they form a percolated network such that they dominate the resistivity measurements leaving small isolated FM domains.

Mn-XMCD measurements provide element specific and surface sensitive magnetic characterization of the NSMO films (Fig. 4(a)–(c)). The TEY detection mode provides surface sensitivity to the top ~5–10 nm of the sample [44] and therefore probes only the main and surface NSMO layers. The Mn-XMCD spectra confirm FM behavior above and below T_N, however, the magnetic signal is smaller in magnitude at 80 K compared to 160 K, consistent with the formation of AFM domains below T_N. Fig. 4(c) and (d) compare the magnetic hysteresis loops acquired by XMCD and bulk magnetometry, respectively at 80 K and 160 K. In both cases, the magnetic field was applied along the [0 0 1] substrate direction and the diamagnetic signal from the STO substrate was subtracted from the bulk magnetometry measurements. The magnetic moment for bulk NSMO is reported to be ~195 emu/cm^3, or 1.18 μ_B/Mn [45,46]; however, the saturation magnetization of the NSMO thin film in Fig. 4(d) is ~135 emu/cm^3 (or 0.82 μ_B/Mn). This difference suggests that the FM/metallic phase and other insulating phases with lower or no net magnetization coexist at the measurement temperatures. In Fig. 4(d) a single magnetic transition is observed at 160 K, while two magnetic transitions are observed at 80 K. This magnetic behavior is consistent with the RXRR fitting that shows that the NSMO film consists of three distinct layers, where this low temperature magnetic phase may correspond with the thin, fully strained layer at the STO substrate interface [47–49]. In contrast, the XMCD hysteresis loops (Fig. 4(c)) display only a single magnetic transition at both temperatures with coercivity values which correspond well with those from the bulk hysteresis loops. Therefore, we propose a model where the surface NSMO layer corresponds to a non-magnetic layer commonly observed in many perovskite oxide thin films [25,47–49], the main NSMO layer displays both the PM/FM and FM/AFM transitions, while the fully strained layer at the substrate interface displays only a PM/FM transition with a reduced T_C.

XLD spectroscopy [50] is one of the few techniques capable of probing AFM order in thin films. In general, XLD spectra are sensitive to any asymmetry in a sample such as crystal-field effects, ferromagnetic anisotropy, orbital ordering, and the charge distribution around AFM moments [51,52]. Therefore, careful design of the experimental geometry is needed to identify the true source(s) of the dichroism. The measurement geometry for the NSMO thin films on (1 1 0)-oriented STO substrates is shown in Fig. 5a. With a 45° incidence angle relative to the sample surface, the *s*- and *p*-polarized X-rays probe the [0 0 1] and [1 0 0] substrate directions, respectively, the latter of which is aligned with the JT distortions which occur to induce the FM-AFM transition. The dichroism is calculated as the difference of the XA spectra obtained from those two directions and shown as a function of temperature in Fig. 5b. A pronounced XLD signal is observed at 80 K (blue curve) and while it decreases in magnitude with increasing temperature, it does not completely disappear at 300 K (red curve). This residual XLD signal likely results from the structural asymmetry of the strained film as it possesses a different line shape compared to the low temperature curves [53–55]. By subtracting the 300 K signal from the 80 K and 160 K curves, we obtain the pure AFM XLD spectra at each temperature (brown and green curves). These two subtracted curves maintain the same spectral shape and only differ in their magnitude, indicating that they have the same origin, i.e. the AFM properties. The XLD intensity of the subtracted curve at 160 K only retains 30% compared to the subtracted curve at 80 K. The fact that the XLD signal does not completely vanish at 160 K, supports the persistence of some AFM domains at this elevated temperature.

In order to investigate the coexistence of the FM and AFM domains at low temperature, XMCD- and XLD-PEEM images were acquired from the same location (Fig. 6) with the incident X-rays oriented along the

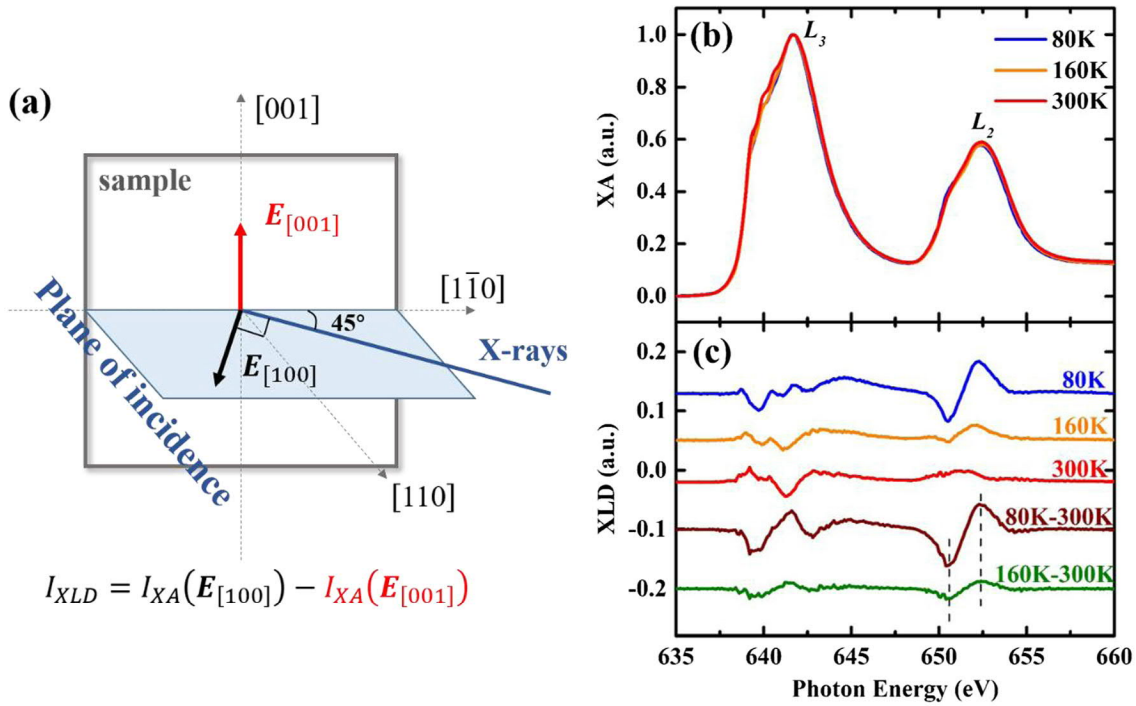

Fig. 5. (a) XLD measurement geometry and Mn (b) XA and (c) XLD spectra taken at 80 K, 160 K, and 300 K. The brown and green curves were obtained by subtracting the 300 K signal from the 80 K and 160 K curves, respectively, in order to show the pure AFM XLD spectrum at each temperature. (For interpretation of the references to colour in this figure legend, the reader is referred to the web version of this article.)

[0 0 1] substrate direction. The sample orientation in the PEEM3 microscope agrees with the XMCD spectroscopy measurements (Fig. 4), but because of the fixed incidence angle (30°) of the instrument, the geometry must differ from the XLD spectroscopy measurements (Fig. 5). The local contrast of an XMCD image follows a cosine dependence between the local magnetization vector and the propagation direction of the incident X-rays. Domains that are aligned parallel/antiparallel to the incident X-ray direction appear with strong white/black contrast. From Fig. 6a, small FM domains (black/white regions) are aligned horizontally in long stripes, separated by long stripes with grey

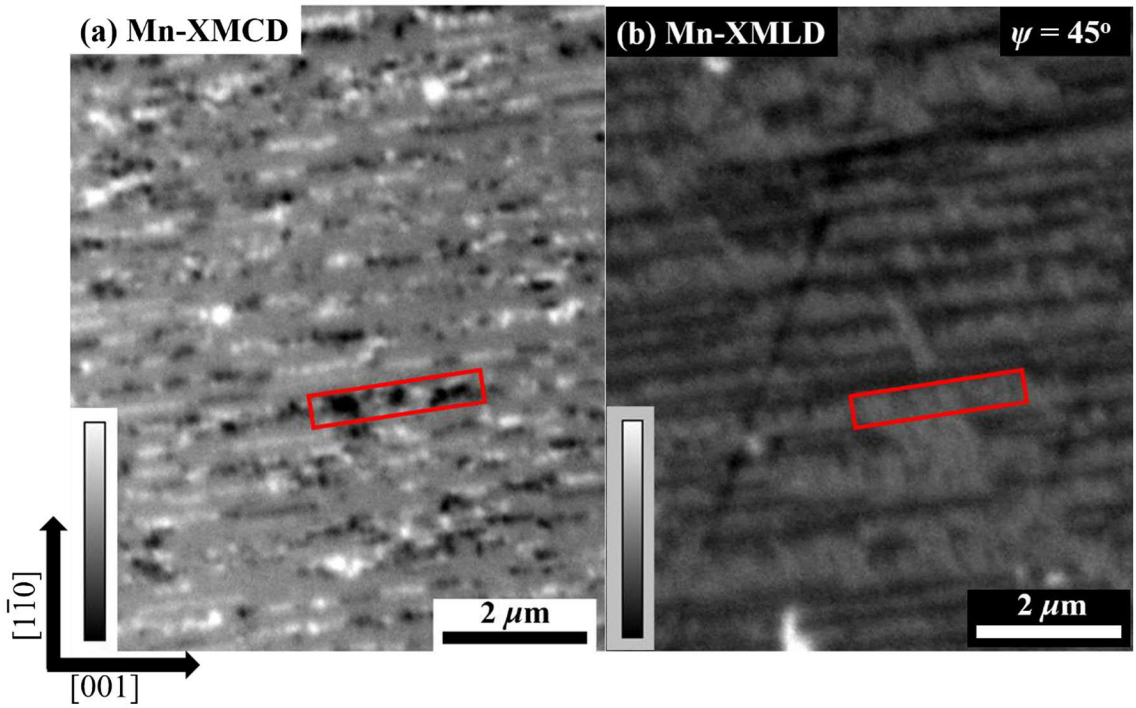

Fig. 6. Mn (a) XMCD- and (b) XLD-PEEM ($\psi = 45°$) images at 110 K taken from the same location. The red rectangle highlights a region with small FM domains which correlates to a gray region in the XLD-PEEM image. (For interpretation of the references to colour in this figure legend, the reader is referred to the web version of this article.)

contrast. The approximate size of the FM domains are 0.5–1 μm. The gray regions can either be domains with magnetization oriented perpendicular to the X-ray incidence direction or non-FM regions.

XLD-PEEM images are used to clarify the nature of these gray regions. The local contrast of an XLD-PEEM image can be described as:

$$I_{XLD}(\theta) = a + b(3cos^2\theta - -1)\langle \boldsymbol{L}^2 \rangle \quad (1)$$

where a and b are material constants, $\boldsymbol{L}$ is the AFM moment, and θ is the angle between $\boldsymbol{L}$ and the $\boldsymbol{E}$-vector of the linearly polarized incident X-rays [56]. In order to fully identify the orientation of the AFM spin axis, images were captured as the orientation of the $\boldsymbol{E}$-vector was varied from p- to s-polarization, i.e. as the polarization angle, ψ varies from 0 to 90°. At each polarization angle, images were collected at two X-ray energies corresponding to the positive/negative peaks in the L_2 XLD signal (dashed lines in Fig. 5c) and the final asymmetry XLD image was calculated. Fig. 6b shows the XLD-PEEM image acquired at $\psi = 45^\circ$ where the domain contrast was the strongest. As with the XMCD-PEEM image, long horizontal stripes are also observed in the XLD-PEEM image with alternating black/gray contrast. Comparing the XMCD- and XLD-PEEM images (e.g. region highlighted by the red square), the FM domains (white/black dots) correspond to gray regions in the XLD-PEEM image, while the gray regions in the XMCD-PEEM image correspond to black regions in the XLD-PEEM image. As shown in Fig. S2, the contrast in the black regions have the expected ψ dependence for AFM domains oriented along the [0 0 1] substrate direction while the gray regions do not show a significant ψ dependence as expected for a FM domain. These images conclusively confirm the coexistence of the FM and AFM domains through the formation of elongated domains oriented along the [0 0 1] substrate direction. PEEM images from other regions of the sample also show the correspondence between the FM and AFM domains, but the directions of the elongated domains vary from location to location across the sample.

4. Conclusions

In summary, the electronic and magnetic transitions of NSMO thin films grown on (1 1 0)-oriented STO substrates were probed using a combination of bulk and synchrotron radiation-based characterization techniques. Under optimized growth conditions, the NSMO film showed both lateral and vertical phase separation, where it consisted of three layers with differing density and magnetic properties. The main NSMO layer constitutes the majority (14.7 nm) of the total film thickness (16.5 nm), and displays bulk-like density. This main layer was fully strained in the in-plane [0 0 1] direction while partially relaxed in the in-plane [1 $\bar{1}$ 0] direction. Resistivity and magnetization measurements revealed that with decreasing temperature, this strain state enabled the NSMO film to transform from a PM/insulating to FM/metallic state at ~197 K and then to an AFM/charge-ordered insulating phase at ~150 K. In order to directly probe the FM and AFM properties of the main NSMO layer, Mn-XMCD/XLD spectroscopy and microscopy were performed as a function of temperature. A carefully designed XLD spectroscopy measurement allowed us to extract the pure AFM signature of the NSMO film. While a clear AFM signature existed below T_N, we found that a proportion of the FM phase remained for temperatures down to 80 K. The lateral coexistence of the FM and AFM phases was directly imaged by X-PEEM where they form extended domains along the [0 0 1] substrate direction. The correspondence between the FM and AFM domains exists across the sample, but the directions of the elongated domains vary from location to location. This understanding of the electronic/magnetic transitions of NSMO in thin film form is necessary to enable its incorporation into next generation memory devices.

Declaration of Competing Interest

The authors declare that they have no known competing financial interests or personal relationships that could have appeared to influence the work reported in this paper.

Acknowledgements

Funding for these experiments was obtained from the National Science Foundation (DMR 1411250). The PLD growth of NSMO films was conducted at the Center for Nanophase Materials Sciences, which is a DOE Office of Science User Facility. This research used resources of the Advanced Light Source, which is a DOE Office of Science User Facility under Contract No. DE-AC02-05CH1123. Use of the Stanford Synchrotron Radiation Lightsource, SLAC National Accelerator Laboratory, is supported by the US Department of Energy, Office of Science, Office of Basic Energy Sciences under Contract No. DE-AC02-76SF00515.

References

[1] S. Parkin, S.-H. Yang, Nat. Nanotechnol. 10 (2015) 195.
[2] A.M. Goforth, P. Klavins, J.C. Fettinger, S.M. Kauzlarich, Inorg. Chem. 47 (2008) 11048.
[3] K. Kuepper, et al., J. Phys.: Condens. Matter 24 (2012) 435602.
[4] C. Şen, G. Alvarez, E. Dagotto, Phys. Rev. Lett. 105 (2010) 097203.
[5] E.J. Wildman, J.M.S. Skakle, N. Emery, A.C. McLaughlin, J. Am. Chem. Soc. 134 (2012) 8766.
[6] J.-C. Lin, et al., Adv. Mater. 28 (2016) 764.
[7] J.-H. Sim, S. Ryee, H. Lee, M.J. Han, Phys. Rev. B 98 (2018) 165114.
[8] J.P. Velev, P.A. Dowben, E.Y. Tsymbal, S.J. Jenkins, A.N. Caruso, Surf. Sci. Rep. 63 (2008) 400.
[9] Z. Sun, et al., Sci. Rep. 3 (2013) 3167.
[10] D.G. Schlom, L.-Q. Chen, X. Pan, A. Schmehl, M.A. Zurbuchen, J. Am. Ceram. Soc. 91 (2008) 2429.
[11] H. Jeen, W.S. Choi, J.W. Freeland, H. Ohta, C.U. Jung, H.N. Lee, Adv. Mater. 25 (2013) 3651.
[12] H. Jeen, et al., Nat. Mater. 12 (2013) 1057.
[13] J. Walter, H. Wang, B. Luo, C.D. Frisbie, C. Leighton, ACS Nano 10 (2016) 7799.
[14] L. Wang, et al., Nat. Mater. 17 (2018) 1087.
[15] M.J. Veit, R. Arras, B.J. Ramshaw, R. Pentcheva, Y. Suzuki, Nat. Commun. 9 (2018) 1458.
[16] D. Lu, D.J. Baek, S.S. Hong, L.F. Kourkoutis, Y. Hikita, H.Y. Hwang, Nat. Mater. 15 (2016) 1255.
[17] R. Kajimoto, H. Yoshizawa, H. Kawano, H. Kuwahara, Y. Tokura, K. Ohoyama, M. Ohashi, Phys. Rev. B 60 (1999) 9506.
[18] J. Chen, Y. Gao, L. Wu, J. Ma, C.-W. Nan, Mater. Res. Lett. 5 (2017) 329.
[19] Y. Lee, et al., Nat. Commun. 6 (2015) 5959.
[20] L.C. Phillips, et al., Sci. Rep. 5 (2015) 10026.
[21] M.M. Savosta, P. Novák, M. Maryško, Z. Jirák, J. Hejtmánek, J. Englich, J. Kohout, C. Martin, B. Raveau, Phys. Rev. B 62 (2000) 9532.
[22] S.S. Pillai, G. Rangarajan, N.P. Raju, A.J. Epstein, P.N. Santhosh, J. Phys.: Condens. Matter 19 (2007) 496221.
[23] H. Kawanaka, A. Noguchi, M. Yokoyama, H. Bando, Y. Nishihara, J. Phys. Conf. Ser. 200 (2010) 032033.
[24] H. Hadipour, S. Fallahi, M. Akhavan, J. Solid State Chem. 184 (2011) 536.
[25] S. Xu, Y. Gu, X. Wu, Solid State Commun. 270 (2018) 119.
[26] S.Y. Jang, N. Nakagawa, S.J. Moon, T. Susaki, K.W. Kim, Y.S. Lee, H.Y. Hwang, K. Myung-Whun, Solid State Commun. 149 (2009) 1760.
[27] S. Ryu, et al., Appl. Phys. Lett. 110 (2017) 261601.
[28] M. Nakamura, Y. Ogimoto, H. Tamaru, M. Izumi, K. Miyano, Appl. Phys. Lett. 86 (2005) 182504.
[29] H. Kuwahara, Y. Tomioka, A. Asamitsu, Y. Moritomo, Y. Tokura, Science 270 (1995) 961.
[30] D. Lu, et al., Phys. Status Solidi 12 (2018) 1700339.
[31] U. Shankar, R. Pandey, A.K. Singh, J. Appl. Phys. 123 (2018) 124301.
[32] G. Lalitha, N. Pavan Kumar, P. Venugopal Reddy, J. Low Temp. Phys. 192 (2018) 133.
[33] N. Kemik, et al., Appl. Phys. Lett. 99 (2011) 201908.
[34] M. Bjorck, G. Andersson, J. Appl. Crystallogr. 40 (2007) 1174.
[35] A. Doran, M. Church, T. Miller, G. Morrison, A.T. Young, A. Scholl, J. Electron. Spectrosc. Relat. Phenom. 185 (2012) 340.
[36] M.A. Torija, M. Sharma, M.R. Fitzsimmons, M. Varela, C. Leighton, J. Appl. Phys. 104 (2008) 023901.
[37] Y. Jia, R.V. Chopdekar, E. Arenholz, A.T. Young, M.A. Marcus, A. Mehta, Y. Takamura, Phys. Rev. B 92 (2015) 094407.
[38] J. Scola, A. Benamar, B. Berini, F. Jomard, Y. Dumont, J. Phys. D Appl. Phys. 50 (2016) 045302.

[39] R. Groenen, J. Smit, K. Orsel, A. Vailionis, B. Bastiaens, M. Huijben, K. Boller, G. Rijnders, G. Koster, APL Mater. 3 (2015) 070701.
[40] S. Yuldashev, H.C. Jeon, H. Im, T. Kang, S.H. Lee, J. Furdyna, Anomalous Hall effect in insulating Ga_ {1 − x} Mn_ {x} As 2004), vol. 70.
[41] B.J. Chen, et al., Phys. Rev. B 90 (2014) 155202.
[42] S.K. Bose, J. Kudrnovský, V. Drchal, I. Turek, Phys. Rev. B 84 (2011) 174422.
[43] T. Ma, et al., Nat. Commun. 8 (2017) 13937.
[44] V.K. Malik, C. Hieu Vo, E. Arenholz, A. Scholl, A.T. Young, Y. Takamura, J. Appl. Phys. 113 (2013) 153907.
[45] R. Venkatesh, M. Pattabiraman, S. Angappane, G. Rangarajan, K. Sethupathi, J. Karatha, M. Fecioru-Morariu, R.M. Ghadimi, G. Guntherodt, Phys. Rev. B 75 (2007) 224415.
[46] S. Kundu, A. Das, T.K. Nath, A.K. Nigam, J. Magn. Magn. Mater. 324 (2012) 823.
[47] M. Sharma, J. Gazquez, M. Varela, J. Schmitt, C. Leighton, Phys. Rev. B 84 (2011) 024417.
[48] J. Curiale, M. Granada, H.E. Troiani, R.D. Sánchez, A.G. Leyva, P. Levy, K. Samwer, Appl. Phys. Lett. 95 (2009) 043106.
[49] S.S.P. Parkin, R. Sigsbee, R. Felici, G.P. Felcher, Appl. Phys. Lett. 48 (1986) 604.
[50] G. van der Laan, B.T. Thole, G.A. Sawatzky, J.B. Goedkoop, J.C. Fuggle, J.-M. Esteva, R. Karnatak, J.P. Remeika, H.A. Dabkowska, Phys. Rev. B 34 (1986) 6529.
[51] G. van der Laan, E. Arenholz, R.V. Chopdekar, Y. Suzuki, Phys. Rev. B 77 (2008) 064407.
[52] C. Aruta, G. Ghiringhelli, V. Bisogni, L. Braicovich, N.B. Brookes, A. Tebano, G. Balestrino, Phys. Rev. B 80 (2009) 014431.
[53] R.V. Chopdekar, J. Heidler, C. Piamonteze, Y. Takamura, A. Scholl, S. Rusponi, H. Brune, L.J. Heyderman, F. Nolting, Eur. Phys. J. B 86 (2013) 241.
[54] D. Pesquera, et al., Phys. Rev. Appl 6 (2016) 034004.
[55] D. Pesquera, G. Herranz, A. Barla, E. Pellegrin, F. Bondino, E. Magnano, F. Sánchez, J. Fontcuberta, Nat. Commun. 3 (2012) 1189.
[56] A. Scholl, et al., Science 287 (2000) 1014.